

1 Dissecting Rate-Limiting Processes in Biomolecular Condensate Exchange Dynamics

2 Ross Kliegman,^{1,*} Eli Kengmana,² Rebecca Schulman,^{2,3,4} and Yaojun Zhang^{1,5,*}

3 ¹*Department of Physics & Astronomy, Johns Hopkins University, Baltimore, Maryland 21218, USA*

4 ²*Chemistry-Biology Interface Program, Johns Hopkins University, Baltimore, Maryland 21218, USA*

5 ³*Department of Chemical & Biomolecular Engineering,*

6 *Johns Hopkins University, Baltimore, Maryland 21218, USA*

7 ⁴*Department of Computer Science, Johns Hopkins University, Baltimore, Maryland 21218, USA*

8 ⁵*Department of Biophysics, Johns Hopkins University, Baltimore, Maryland 21218, USA*

9 (Dated: May 16, 2025)

An increasing number of biomolecules have been shown to phase-separate into biomolecular condensates — membraneless subcellular compartments capable of regulating distinct biochemical processes within living cells. The speed with which they exchange components with the cellular environment can influence how fast biochemical reactions occur inside condensates and how fast condensates respond to environmental changes, thereby directly impacting condensate function. While Fluorescence Recovery After Photobleaching (FRAP) experiments are routinely performed to measure this exchange timescale, it remains a challenge to distinguish the various physical processes limiting fluorescence recovery and identify each associated timescale. Here, we present a reaction-diffusion model for condensate exchange dynamics and show that such exchange can differ significantly from that of conventional liquid droplets due to the presence of a percolated molecular network, which gives rise to different mobility species in the dense phase. In this model, exchange can be limited by diffusion of either the high- or low-mobility species in the dense phase, diffusion in the dilute phase, or the attachment/detachment of molecules to/from the network at the surface or throughout the bulk of the condensate. Through a combination of analytic derivations and numerical simulations in each of these limits, we quantify the contributions of these distinct physical processes to the overall exchange timescale. Demonstrated on a biosynthetic DNA nanostar system, our model offers insight into the predominant physical mechanisms driving condensate material exchange and provides an experimentally testable scaling relationship between the exchange timescale and condensate size. Interestingly, we observe a newly predicted regime in which the exchange timescale scales nonquadratically with condensate size.

10 INTRODUCTION

11 Recent discoveries have found that living cells exploit a
12 type of phase transition known as liquid-liquid phase sep-
13 aration for intracellular organization. This new paradigm
14 challenges the traditional textbook view of the cell that
15 organelles are mostly membrane-bound. Rather, subcel-
16 lular structures can take the form of dynamic, liquid-like
17 networks of molecules called “biomolecular condensates”
18 [1, 2]. These condensates are dense assemblies of dis-
19 tinct proteins and nucleic acids that are driven by mul-
20 tivalent interactions to segregate out of the intracellu-
21 lar milieu. They enable functions vital for life, includ-
22 ing gene regulation [3–5], signal transduction [6–8], and
23 stress response [9–11], and when misregulated, they have
24 been implicated in various diseases, most notably neu-
25 rodegeneration [12–14] and cancer [15–18]. Understand-
26 ing how condensates form and evolve over time in cells
27 can deepen our physical understanding of emergent self-
28 organization in biological systems and potentially inform
29 human health.

30 The earliest measurements of condensate physical
31 properties were made on *Caenorhabditis elegans* germ
32 granules, or P granules, which were shown to be liquid-
33 like — they constantly fuse with each other, flow under
34 applied shear stresses, and undergo internal rearrange-

35 ment [19]. Often essential for their biological functions,
36 the liquid-like nature of condensates enables them to ex-
37 change materials with the surrounding dilute phase. For
38 instance, metabolic condensates, such as purinosomes
39 [20, 21], are enriched in enzymes, substrates, and other
40 biomolecules involved in specific metabolic pathways [22].
41 Regulating metabolic activity in condensates requires not
42 only that reactants can partition into them, but also that
43 products can later escape. However, with viscosities or-
44 ders of magnitude larger than conventional oil droplets
45 [23], condensates are thought to experience slow internal
46 diffusion, limiting the exchange dynamics. More broadly,
47 the speed of material exchange can influence the response
48 of condensates to environmental changes, as well as the
49 number, size, and spatial distribution of condensates via
50 Ostwald ripening [24, 25]. Collectively, these effects can
51 impact condensate function, motivating a need for tools
52 to accurately measure and interpret the exchange dynam-
53 ics.

54 The timescales of molecular exchange are commonly
55 measured with an experimental technique known as Flu-
56 orescence Recovery After Photobleaching (FRAP) [26–
57 29]. In a typical FRAP experiment, fluorescently labeled
58 molecules are photobleached within a region of interest
59 (ROI) upon irradiation with a high-intensity laser. The
60 fluorescence intensity in the ROI then recovers over time
61 due to molecular exchange with the surroundings until

62 constant intensity is eventually restored. Photobleaching
 63 can be performed on a subregion within a droplet, known
 64 as partial FRAP, or on an entire droplet, known as full
 65 FRAP. Exchange dynamics have been studied in a range
 66 of experimental condensate systems [6, 10, 30–33], and
 67 complementary theories were developed to extract mean-
 68 ingful physical quantities from measured fluorescence re-
 69 covery curves [34–37]. Notably, all of these studies made
 70 an assumption that the exchange dynamics were limited
 71 by molecular diffusion. However, recent studies suggest
 72 that condensate material exchange can also be limited by
 73 other physical processes due to the complexity of molecu-
 74 lar interactions [38–42], e.g., interface resistance [41, 42].

75 The exchange dynamics of condensates are ultimately
 76 determined by the constituent biomolecules and their
 77 microscopic structures and interactions. While phase-
 78 separating molecules often exhibit a complex set of in-
 79 teractions, they generally conform to a “sticker-spacer”
 80 architecture [43, 44], where “stickers” represent residues,
 81 nucleotide segments, or larger folded domains capable of
 82 forming reversible physical cross-links that drive phase
 83 separation, and “spacers” exclude volume and connect
 84 the stickers to form polymers. In the sticker-spacer
 85 framework, it follows that phase-separating molecules of-
 86 ten form dynamically restructuring networks that go be-
 87 yond traditional liquid-liquid phase separation (Fig. 1a),
 88 sometimes referred to as “phase separation coupled to
 89 percolation” [45, 46]. In the modified physical picture
 90 (Fig. 1b), attachment/detachment of molecules to/from
 91 the percolated network intuitively gives rise to differ-
 92 ent mobility populations within the condensate for the
 93 same type of molecule. The low-mobility population (re-
 94 ferred to as “species 1”) represents molecules bound to
 95 the network, and the high-mobility population (referred
 96 to as “species 2”) represents freely diffusing molecules
 97 detached from the network. Indeed, multiple mobility
 98 populations have been reported in the dense phase of an
 99 *in vitro* reconstituted postsynaptic density system [47]
 100 as well as single-component A1-LCD condensates [48].
 101 However, a theory to interpret such experimental results
 102 has been missing. Here, we present a model that accounts
 103 for a condensate’s molecular network and discuss some of
 104 its implications for the exchange timescale.

105 RESULTS

106 A reaction-diffusion model for condensate exchange 107 dynamics

108 To explore how the percolated network and the pres-
 109 ence of two mobility species impact the condensate ex-
 110 change timescale, we first develop a reaction-diffusion
 111 model for a phase-separated system at equilibrium. As-
 112 suming a spherical condensate, we describe the recov-
 113 ery dynamics of a bleached condensate (equivalent to the

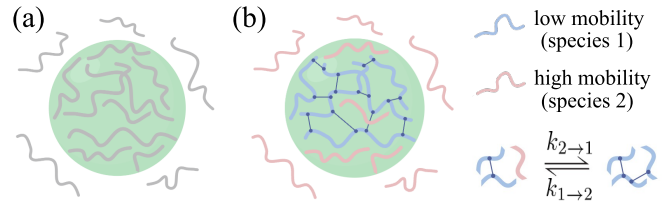


FIG. 1. Schematics of a condensate in (a) the conventional model, which assumes uniform molecular mobility inside and outside the condensate (depicted in grey), and (b) our proposed model, in which binding kinetics with the molecular network can give rise to multiple mobilities for the same molecule inside the condensate. Connected blue molecules are bound to the network, whereas individual pink molecules are freely diffusing. By attaching and detaching, the two mobility species can convert between one another with rates $k_{2\rightarrow 1}$ and $k_{1\rightarrow 2}$, respectively.

114 exchange dynamics) by the following coupled reaction-
 115 diffusion equations:

$$\frac{\partial c_1}{\partial t} = \nabla \cdot \left[D_1 \left(\nabla c_1 - c_1 \frac{\nabla c_1^{\text{eq}}}{c_1^{\text{eq}}} \right) \right] + k (c_1^{\text{eq}} c_2 - c_2^{\text{eq}} c_1), \quad (1)$$

$$\frac{\partial c_2}{\partial t} = \nabla \cdot \left[D_2 \left(\nabla c_2 - c_2 \frac{\nabla c_2^{\text{eq}}}{c_2^{\text{eq}}} \right) \right] - k (c_1^{\text{eq}} c_2 - c_2^{\text{eq}} c_1), \quad (2)$$

116 where $c_1(r, t)$ and $c_2(r, t)$ are the bleached concentrations
 117 of species 1 and 2, respectively, $D_1(r)$ and $D_2(r)$ are
 118 their position-dependent diffusion coefficients, $c_1^{\text{eq}}(r)$ and
 119 $c_2^{\text{eq}}(r)$ are their equilibrium concentration profiles, and k
 120 is a parameter that encodes how fast molecules convert
 121 between species. The coordinate r is the distance from
 122 the center of the condensate, and t denotes the time.

123 In Eqs. (1) and (2), the first terms on the right
 124 represent conventional Fickian diffusion in a concentra-
 125 tion gradient, and the second terms represent excess
 126 chemical potentials that drive molecules towards nonuni-
 127 form equilibrium concentration profiles. The third and
 128 fourth terms account for mobility switching due to bind-
 129 ing/unbinding with the network. Molecules can attach
 130 to the percolated network and lower their mobility with
 131 a rate $k_{2\rightarrow 1}(r)$, and detach from the network and regain
 132 higher mobility with a rate $k_{1\rightarrow 2}(r)$. Detailed balance
 133 requires that the fluxes of association ($c_2 k_{2\rightarrow 1}$) and dis-
 134 sociation ($c_1 k_{1\rightarrow 2}$) are equal at equilibrium, which allows
 135 us to characterize these rates in terms of a single pa-
 136 rameter, $k(r) \equiv k_{2\rightarrow 1}(r)/c_1^{\text{eq}}(r) = k_{1\rightarrow 2}(r)/c_2^{\text{eq}}(r)$. For
 137 simplicity, we assume k to be a constant, independent of
 138 the location of the molecule. The system reaches equi-
 139 librium when $c_1(r, t)/c_1^{\text{eq}}(r) = c_2(r, t)/c_2^{\text{eq}}(r) = f_b$, where
 140 the constant f_b is the fraction of total molecules that are
 141 bleached.

142 Analogous to a FRAP experiment, we set the initial

144 condition to be

$$c_i(r, 0) = \begin{cases} c_i^{\text{eq}}(r), & r \leq R; \\ 0, & r > R \end{cases} \quad (3)$$

145 for a fully bleached droplet, where $i = 1, 2$, and R is the
146 droplet radius. We impose no-flux boundary conditions
147 to conserve total particle number in the system:

$$\left. \frac{\partial c_i(r, t)}{\partial r} \right|_{r=0} = \left. \frac{\partial c_i(r, t)}{\partial r} \right|_{r=+\infty} = 0. \quad (4)$$

148 Upon solving for $c_1(r, t)$ and $c_2(r, t)$, we can obtain a nor-
149 malized brightness curve $I(t)$ for the fraction of molecules
150 inside the droplet that are unbleached at a time t :

$$I(t) = 1 - \frac{\int_0^R [c_1(r, t) + c_2(r, t)] r^2 dr}{\int_0^R [c_1^{\text{eq}}(r) + c_2^{\text{eq}}(r)] r^2 dr}. \quad (5)$$

151 Finally, the characteristic timescale τ of the exchange
152 dynamics is identified by fitting $I(t)$ to an exponential
153 function of the form $1 - e^{-t/\tau}$.

154 Quantifying the timescales of rate-limiting processes

155 Analytical derivations

156 A proxy for condensate material exchange, fluores-
157 cence recovery in a bleached droplet is a multi-step
158 process involving dilute-phase diffusion, network attach-
159 ment/detachment, and dense-phase diffusion. We outline
160 the rate-limiting steps of FRAP recovery in Fig. 2. First,
162 an unbleached molecule must diffuse through the dilute
163 phase to reach the droplet surface. In the limit of low
164 dilute-phase concentration, we derive the dilute-phase

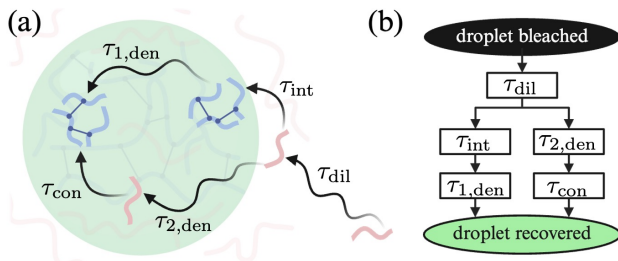


FIG. 2. Schematic (a) and flowchart (b) of rate-limiting pro-
cesses in the exchange dynamics of biomolecular condensates.
In order for fluorescence to recover in a bleached droplet, an
unbleached molecule first has to diffuse in the dilute phase
with a timescale τ_{dil} until it encounters the droplet, and then
either attach to the network at the surface with a timescale
 τ_{int} and diffuse into the droplet with a timescale $\tau_{1,\text{den}}$, or
diffuse through the network mesh inside the droplet with
a timescale $\tau_{2,\text{den}}$ and subsequently attach to the network
within the droplet bulk with a timescale τ_{con} .

165 diffusion timescale τ_{dil} shown in Eq. (6a). Next, in the
166 limit of low dense-phase concentration of species 2, the
167 unbleached molecule is more likely to enter the droplet by
168 attaching to the network at the droplet interface and sub-
169 sequently diffusing into the bulk dense phase as species
170 1. In this case, if interfacial attachment/detachment is
171 rate-limiting, we derive the interface-limited timescale
172 τ_{int} shown in Eq. (6b), whereas if dense-phase diffusion of
173 species 1 is rate-limiting, we derive the timescale $\tau_{1,\text{den}}$
174 shown in Eq. (6c). Finally, for sufficiently high dense-
175 phase concentration of species 2, the unbleached molecule
176 is more likely to enter the droplet by passing through
177 the pores of the network and diffusing around the dense
178 phase as species 2, which then attaches to and detaches
179 from the network throughout the bulk of the droplet.
180 In this case, if dense-phase diffusion of species 2 is rate-
181 limiting, we derive the timescale $\tau_{2,\text{den}}$ shown in Eq. (6d),
182 whereas if attachment/detachment throughout the bulk
183 of the droplet is rate-limiting, we derive the conversion-
184 limited timescale τ_{con} shown in Eq. (6e). Detailed deriva-
185 tions of each timescale are provided in the Supplemental
186 Material [49].

$$\tau_{\text{dil}} = \frac{R^2 c_{1,\text{den}}}{3D_{2,\text{dil}} c_{2,\text{dil}}}, \quad (6a)$$

$$\tau_{\text{int}} = \frac{R}{3k c_{2,\text{dil}} \delta_{\text{eff}}}, \quad (6b)$$

$$\tau_{1,\text{den}} = \frac{R^2}{\pi^2 D_{1,\text{den}}}, \quad (6c)$$

$$\tau_{2,\text{den}} = \frac{R^2 c_{1,\text{den}}}{\pi^2 D_{2,\text{den}} c_{2,\text{den}}}, \quad (6d)$$

$$\tau_{\text{con}} = \frac{1}{k c_{2,\text{den}}}. \quad (6e)$$

187 $D_{1,\text{den}}$ and $D_{2,\text{den}}$ are the dense-phase diffusion coeffi-
188 cients of species 1 and 2, respectively, $c_{1,\text{den}}$ and $c_{2,\text{den}}$
189 are the dense-phase equilibrium concentrations of species
190 1 and 2, respectively, $D_{2,\text{dil}}$ is the dilute-phase diffusion
191 coefficient of species 2, $c_{2,\text{dil}}$ is the dilute-phase equilib-
192 rium concentration of species 2, and δ_{eff} is the effective
193 width of the droplet interface. We note that $c_{1,\text{dil}} = 0$ as
194 there is no percolated network in the dilute phase. The
195 above derivations also assume $c_{2,\text{den}} \ll c_{1,\text{den}}$ as species
196 1 is energetically favored and therefore more abundant.

197 Each physical process has a distinct timescale that
198 scales with droplet size differently. Specifically, the
199 diffusion-limited processes in both dense and dilute
200 phases are associated with timescales that naturally
201 scale as R^2/D [Eqs. (6a), (6c), and (6d)]. The fac-
202 tors $c_{1,\text{den}}/c_{2,\text{dil}}$ and $c_{1,\text{den}}/c_{2,\text{den}}$ in Eqs. (6a) and (6d)
203 account for replacing bleached molecules of concentra-
204 tion $c_{1,\text{den}}$ with unbleached molecules of concentrations
205 $c_{2,\text{dil}}$ and $c_{2,\text{den}}$, respectively. The interfacial timescale
206 [Eq. (6b)] accounts for exchange of a volume of molecules
207 ($\sim R^3$) over a surface ($\sim R^2$) and is therefore linear in

208 R . Lastly, the conversion-limited timescale [Eq. (6e)] is
 209 independent of R , which arises due to rate-limiting detach-
 210 ment of bleached molecules throughout the bulk of the
 211 dense phase, i.e., the lifetime of a molecule in the net-
 212 work [given by $1/k_{1 \rightarrow 2} = 1/(kc_{2,\text{den}})$]. Once detached,
 213 these molecules can quickly escape the droplet, allowing
 214 unbleached molecules to attach to the network.

215 Putting together the rate-limiting steps, we propose
 216 the following expression for the overall timescale of fluo-
 217 rescence recovery:

$$\tau = \tau_{\text{dil}} + \left[(\tau_{\text{int}} + \tau_{1,\text{den}})^{-1} + (\tau_{2,\text{den}} + \tau_{\text{con}})^{-1} \right]^{-1}, \quad (7)$$

218 where following diffusion in the dilute phase, two compet-
 219 ing modes of recovery occur in parallel, each a sequence
 220 of two steps (Fig. 2b). It is worth noting that by set-
 221 ting $c_{2,\text{den}} = 0$ in Eq. (7), i.e., assuming a single mobil-
 222 ity species inside the droplet, we recover results of our
 223 previous study [41]. In particular, Eq. (6b) arises due to
 224 the ‘‘interface resistance’’ of the droplet, which was previ-
 225 ously modeled with a phenomenological parameter κ , but
 226 now acquires a clear physical meaning: τ_{int} is governed
 227 by the molecular attachment/detachment at the droplet
 228 interface. For $c_{2,\text{den}} > 0$, the emergence of a new path-
 229 way in Fig. 2 leads to two previously unrecognized terms
 230 in the recovery time [Eq. (7)], resulting in a complex de-
 231 pendence of τ on the droplet radius R . We demonstrate
 232 this complex dependence via numerical simulations and
 233 FRAP experiments on DNA nanostar droplets below.

Numerical simulations

235 In the previous section, we derived the timescale of
 236 fluorescence recovery by analytically solving the reaction-
 237 diffusion system described by Eqs. (1-5) in various limits.
 238 Here, we numerically verify these timescales and visual-
 239 ize the different FRAP signatures in each rate-limiting
 240 case. Specifically, we first specify the functional forms
 241 of equilibrium concentrations and diffusion coefficients
 242 with sharp but smooth transitions at the droplet inter-
 243 face ($r = R$) over a finite width $\sim l$:

$$c_i^{\text{eq}}(r) = \frac{c_{i,\text{dil}} - c_{i,\text{den}}}{2} \tanh\left(\frac{r - R}{l}\right) + \frac{c_{i,\text{dil}} + c_{i,\text{den}}}{2},$$

$$D_i(r) = \frac{D_{i,\text{dil}} - D_{i,\text{den}}}{2} \tanh\left(\frac{r - R}{l}\right) + \frac{D_{i,\text{dil}} + D_{i,\text{den}}}{2},$$

244 which are consistent with equilibrium solutions of the
 245 Cahn-Hilliard equation [50]. The initial and bound-
 246 ary conditions are given by Eqs. (3) and (4), respec-
 247 tively, except that the boundary at $r = +\infty$ is replaced
 248 by $r = r_{\text{max}}$ for the finite size of the system. We
 249 then solve Eqs. (1) and (2) numerically under spher-
 250 ical symmetry using the *pdepe* function in MATLAB,
 251 which employs finite-difference spatial discretization with

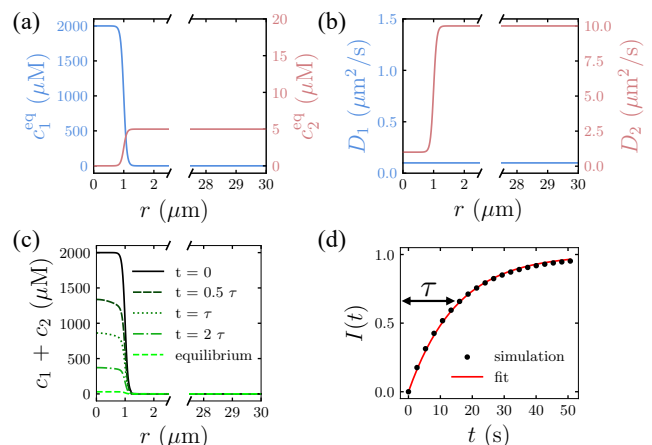


FIG. 3. Representative simulation in a dilute-phase diffusion-
 limited scenario (parameters from top row in Table I). (a)
 Equilibrium concentration profiles and (b) diffusivity profiles
 for species 1 and 2. (c) Simulated radial concentration profiles
 of the bleached molecules for a few illustrative times. (d) Sim-
 ulated brightness curve with exponential fit using nonlinear
 least squares. Simulations were performed with radial step
 size $dr = 20$ nm over a system size of $r_{\text{max}} = 30$ μm for 1000
 timepoints (the solver dynamically selects both the timestep
 and formula).

252 a variable-step, variable-order solver for time integration
 253 [51]. The numerical solutions for $c_1(r, t)$ and $c_2(r, t)$ are
 254 used to compute a brightness curve in accordance with
 255 Eq. (5), which is subsequently fitted to extract the recov-
 256 ery timescale.

261 We show an example where the FRAP recovery is
 262 limited by dilute-phase diffusion in Fig. 3. Guided by
 263 Eq. (7), we choose physiological parameters of condensate
 264 systems [23, 52, 53] that lead to $\tau \approx \tau_{\text{dil}}$ (Table I). The
 265 numerically extracted relaxation time $\tau = 15.1$ s of an
 266 $R = 1$ μm droplet is indeed close to the theory prediction
 267 of $\tau_{\text{dil}} = 13.3$ s. We repeat a similar procedure for various
 268 parameter sets in which the timescale of fluorescence recov-
 269 ery is limited by interfacial attachment/detachment,
 270 dense-phase diffusion of the low-mobility species, dense-
 271 phase diffusion of the high-mobility species, and attach-
 272 ment/detachment throughout the bulk of the condensate,
 273 totaling five cases. Simulated spatial fluorescence recov-
 274 ery profiles for each of these cases are shown in Fig. 4
 275 with parameters listed in Table I. The two cases of dense-
 276 phase diffusion-limited recovery (rows c and d) can read-
 277 ily be distinguished by the pronounced gradient present
 278 due to unbleached molecules gradually diffusing into the
 279 condensate and bleached ones diffusing out, whereas the
 280 remaining three cases all display a uniform recovery. De-
 281 tails of the numerical implementation and fitting are pro-
 282 vided in the Supplemental Material [49].

283 Based on Eq. (6), condensate recovery timescales are
 284 expected to follow different scaling laws in different

TABLE I. Parameter choice for numerical simulations of five rate-limiting cases.

Case	$c_{1,\text{den}}$ (μM)	$c_{1,\text{dil}}$ (μM)	$c_{2,\text{den}}$ (μM)	$c_{2,\text{dil}}$ (μM)	$D_{1,\text{den}}$ ($\mu\text{m}^2/\text{s}$)	$D_{1,\text{dil}}$ ($\mu\text{m}^2/\text{s}$)	$D_{2,\text{den}}$ ($\mu\text{m}^2/\text{s}$)	$D_{2,\text{dil}}$ ($\mu\text{m}^2/\text{s}$)	l (μm)	k ($\mu\text{M}^{-1}\text{s}^{-1}$)
$\tau \approx \tau_{\text{dil}}$	2000	0	0	5	0.1	0.1	1	10	0.1	1
$\tau \approx \tau_{\text{int}}$	1000	0	0	10	0.02	0.02	1	50	0.1	0.005
$\tau \approx \tau_{1,\text{den}}$	1000	0	0	10	0.02	0.02	1	50	0.1	1
$\tau \approx \tau_{2,\text{den}}$	1995	0	5	10	5×10^{-5}	5×10^{-5}	0.1	50	0.01	0.005
$\tau \approx \tau_{\text{con}}$	980	0	20	10	0.02	0.02	1	50	0.05	1×10^{-4}

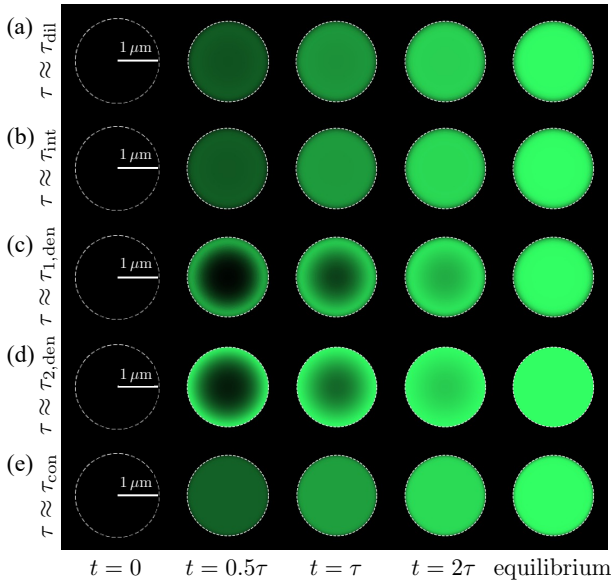


FIG. 4. Simulated FRAP recovery profiles when fluorescence recovery is limited by (a) dilute-phase diffusion, (b) interfacial attachment/detachment, (c) dense-phase diffusion of species 1, (d) dense-phase diffusion of species 2, and (e) attachment/detachment throughout the bulk of the condensate. Green indicates fluorescent molecules and black indicates bleached molecules. Simulations were performed with radial step sizes $1/5$ of the interface width l , and the system size was $r_{\text{max}} = 30 \mu\text{m}$. 1000 timepoints were recorded over 4τ -long runtimes.

rate-limiting cases. As shown in Fig. 5, the different timescales indeed scale differently with droplet size *in silico* as well. When diffusive processes are rate-limiting, the scaling law is quadratic; when the interfacial flux is rate-limiting, the scaling law is linear; and when the network attachment/detachment throughout the droplet is rate-limiting, the scaling law is independent of droplet size.

Application to a DNA nanostar system

Finally, we sought to employ our theory in an experimental system composed of DNA nanostars — a model system for investigating biomolecular condensation. Thanks to advances in artificial DNA synthesis

techniques, DNA nanostars offer highly programmable interactions: binding specificity and affinity can be tuned via the sequence and length of single-stranded overhangs, and valence via the number of arms. These features collectively enable a diverse range of phase behaviors [54–57]. Our DNA nanostars are composed of three arms of double-stranded DNA, each with a short tail of single-stranded DNA known as a “sticky end” due to its propensity to Watson-Crick base-pair with complementary strands (Fig. 6a). The sticky ends make these nanostars readily phase-separable, and micron-sized droplets can be seen with confocal microscopy. Details about sequences and sample preparation are given in the Supplemental Material [49].

DNA nanostars form porous networks inside their condensates, with the mesh size determined by the engineered arm length and valence [59, 60]. This property makes them a prime system in which to observe the new mode of recovery discussed above: nearby molecules may penetrate the droplet surface and diffuse freely within the droplet before attaching to the network. If this were the dominant recovery mechanism, we would expect to observe conversion-limited recovery for small droplets, transitioning to diffusion-limited recovery for large droplets. Upon performing FRAP on nanostar droplets of varying sizes (Fig. 6b), we noticed that the recovery curves and hence the recovery timescales were nearly identical for droplets of small sizes ($R \lesssim 1.5 \mu\text{m}$), despite spanning nearly a twofold size range (Fig. 6c and 6d). This observation aligns with the scaling behavior of conversion-limited recovery. If the recovery of these droplets were diffusion-limited, whether by dilute-phase diffusion, species 1 dense-phase diffusion, or species 2 dense-phase diffusion, we would expect nearly a fourfold difference in exchange timescale. For larger droplets, we see a quadratic scaling that plateaus at the conversion-limited timescale (Fig. 6d). Upon fitting the data with the shifted quadratic function $\tau = a + bR^2$, we find the constants a and b are well-constrained: $a = 145.0 \pm 5.6 \text{ s}$ and $b = 14.1 \pm 0.7 \mu\text{m}^{-2}\text{s}$.

As suggested by our theory, the plateau regime arises because the recovery is conversion-limited, i.e., $\tau_{\text{con}} = 1/(kc_{2,\text{den}}) = a$. Nanostar droplets are porous, with a measured pore size comparable to the arm length. It has been reported that the partition coefficient for 70

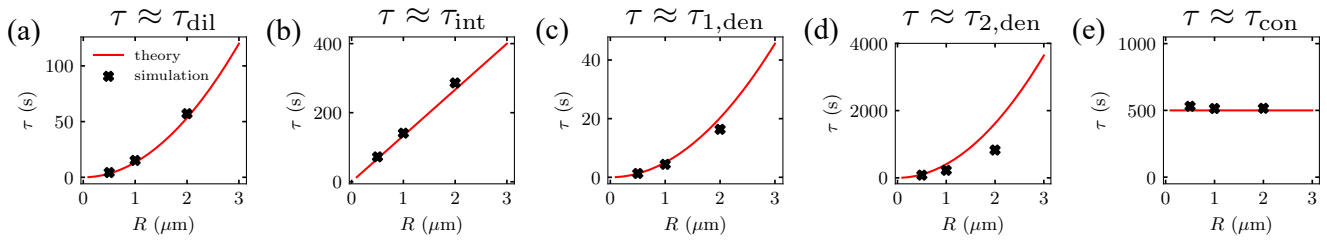


FIG. 5. Theoretical and simulated scaling laws show good agreement in each rate-limiting case: (a) dilute-phase diffusion-limited timescale scales with R^2 , (b) interface-limited timescale scales with R , (c) dense-phase diffusion-limited timescale (species 1) scales with R^2 , (d) dense-phase diffusion-limited timescale (species 2) scales with R^2 , and (e) conversion-limited timescale is independent of R . Red curves: theoretical predictions from Eq. (6) using parameters from Table I; black crosses: simulation results for droplets of radii $R = 0.5 \mu\text{m}$, $1 \mu\text{m}$, and $2 \mu\text{m}$.

344 kDa dextran (hydrodynamic radius 6 nm) is about 0.3
 345 – 0.6 in such systems [59, 60]. Given that our nanos-
 346 tars have a hydrodynamic radius (5 – 7 nm) similar
 347 to that of dextran, we expect the unbound species of
 348 nanostars to partition in these nanostar droplets to a
 349 similar extent as the dextran. Assuming a partition co-
 350 efficient of 0.5 and dilute-phase concentration of $1 \mu\text{M}$,
 351 $c_{2,\text{den}} \approx 0.5 c_{2,\text{dil}} \approx 0.5 \mu\text{M}$, and the rate of nanostar
 352 attachment inside the condensate can be estimated as
 353 $k = 1/(a c_{2,\text{den}}) \approx 0.014 \mu\text{M}^{-1}\text{s}^{-1}$. This rate appears to
 354 be much lower than the reported on-rate for nanostars
 355 in dilute solution, which ranges from 0.1 to $1 \mu\text{M}^{-1}\text{s}^{-1}$
 356 [61]. The discrepancy likely arises because we have mod-
 357 eled the attachment flux as $k c_1^{\text{eq}} c_2$ in Eq. (1), implicitly
 358 assuming that every species 1 nanostar in the percolated
 359 network can bind to freely diffusing species 2 nanostars.
 360 However, many nanostars in the network may already be
 361 in a fully bound state or spatially occluded and thus un-
 362 available for binding, leading to a smaller apparent k . If
 363 we take these numbers seriously, this would suggest that
 364 about 90% of nanostars are not available for binding in
 365 the droplet.

366 Beyond the plateau regime, comparing the interface-
 367 limited timescale with the conversion-limited timescale
 368 gives the relation $\tau_{\text{int}} = \tau_{\text{con}} R c_{2,\text{den}} / (3 \delta_{\text{eff}} c_{2,\text{dil}})$. Also,
 369 nanostar condensates have a surface tension around
 370 $1 \mu\text{N/m}$ [56], which corresponds to an effective inter-
 371 face width $\delta_{\text{eff}} \approx 30 \text{ nm}$. Therefore, a droplet of radi-
 372 us R (in μm) would have an interface-limited timescale
 373 $\tau_{\text{int}} \approx 800 R \text{ s}$. Since this is much longer than the recovery
 374 times measured experimentally, we argue that the con-
 375 ventional pathway of attaching at the droplet interface
 376 followed by diffusion through the network is not the fa-
 377 vored mode of recovery for the nanostar droplets studied
 378 here. This leads to a reduced expression for the overall
 379 relaxation time from Eq. (7): $\tau = \tau_{\text{dil}} + \tau_{2,\text{den}} + \tau_{\text{con}}$.
 380 While $\tau_{\text{con}} = a$ sets the plateau value, both τ_{dil} and
 381 $\tau_{2,\text{den}}$ scale with R^2 and can contribute to the prefactor
 382 $b = c_{1,\text{den}} / (3 D_{2,\text{dil}} c_{2,\text{dil}}) + c_{1,\text{den}} / (\pi^2 D_{2,\text{den}} c_{2,\text{den}})$. Tak-
 383 ing $c_{1,\text{den}} = 200 \mu\text{M}$, $c_{2,\text{dil}} = 1 \mu\text{M}$, $c_{2,\text{den}} = 0.5 \mu\text{M}$,

384 and $D_{2,\text{dil}} = 20 \mu\text{m}^2/\text{s}$ (from the Stokes-Einstein rela-
 385 tion) [58, 62], we estimate $D_{2,\text{den}} \approx 4 \mu\text{m}^2/\text{s}$.

386 DISCUSSION

387 A hallmark of biomolecular condensates is their dy-
 388 namic exchange of materials with their surroundings, a
 389 feature often crucial to their function. In this work, we
 390 developed a novel reaction-diffusion model to describe
 391 condensate exchange dynamics and explored how such
 392 dynamics can deviate from those of conventional liquid
 393 droplets due to the formation of a percolated network in
 394 the condensate. We found that in the presence of two
 395 mobility states, material exchange can be accelerated via
 396 a new pathway in which molecules pass through the pores
 397 of the meshwork and attach/detach directly in the con-
 398 densate interior. Notably, this pathway leads to a new
 399 regime where the exchange timescale becomes indepen-
 400 dent of condensate size, a prediction we confirmed using
 401 FRAP experiments on DNA nanostar condensates.

402 In this study, we focused on the exchange dynamics
 403 of *in vitro* single-component condensates and approxi-
 404 mated a condensate as a two-state system at equilibrium.
 405 Molecules inside biological condensates, even in single-
 406 component systems, are likely to exhibit a broad range
 407 of mobilities due to the complexity of underlying interac-
 408 tions [47, 48]. A natural next step would be to incorpo-
 409 rate more mobility states into the model. Nevertheless, a
 410 concise two-state model can capture the essential physi-
 411 cal principles underlying condensate exchange dynamics
 412 while remaining analytically tractable.

413 The developed reaction-diffusion model can also be
 414 readily extended to describe multi-component systems.
 415 Condensates in living cells are complex assemblies of dis-
 416 tinct proteins and nucleic acids, which generally employ
 417 a scaffold-client framework [45, 46]. While our model fo-
 418 cused on the exchange dynamics of scaffold molecules,
 419 the same mathematical framework applies to client dy-
 420 namics, where client molecules can bind (low mobil-

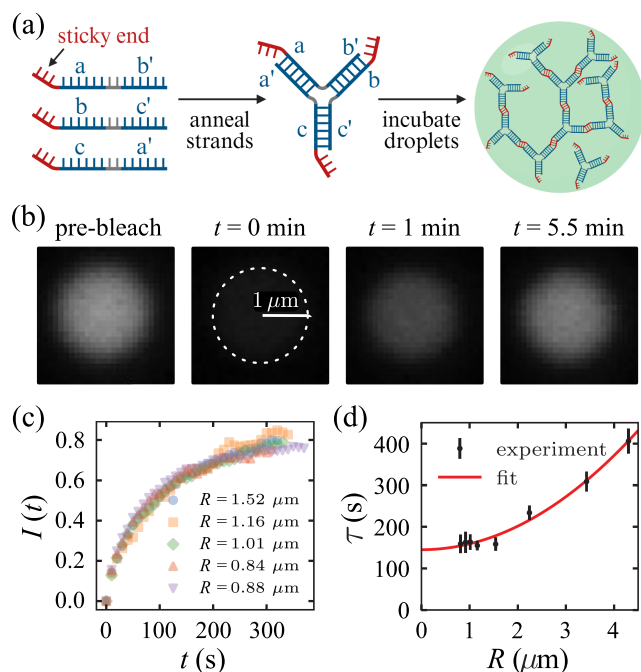


FIG. 6. Experimental characterization of exchange dynamics in DNA nanostar condensates. (a) Nanostar schematic. The Y-shaped nanostar has 16-bp double-stranded arms shown in blue, sticky ends with the palindromic sequence 5'-GCTAGC-3' in red, and non-complementary linkers with the sequence 5'-TT-3' in gray that confer angular flexibility between arms. The nanostars were first annealed in a low-salt solution, then added to a higher salt solution at 37 °C to incubate condensates, following the same protocol as in [58]. (b) Representative snapshots from a FRAP experiment of an $R = 1 \mu\text{m}$ nanostar droplet. (c) FRAP recovery curves for droplets of small sizes ($R \lesssim 1.5 \mu\text{m}$). (d) Exchange timescale versus droplet radius for all droplets, fitted with a shifted quadratic function of the form $\tau = a + bR^2$, where $a = 145.0 \pm 5.6 \text{ s}$ and $b = 14.1 \pm 0.7 \mu\text{m}^{-2}\text{s}$. Error bars are defined at 3σ .

ity)/unbind (high mobility) to/from an equilibrated scaffold network. The model can also be used to predict the dynamics of condensates in the cell nucleus, where molecules diffusing within the condensate are also capable of binding to/unbinding from DNA [63, 64].

The newly discovered pathway involves molecules passing through the pores of the meshwork and attaching/detaching directly within the condensate. In which systems, and for which molecules, would this pathway be favored and experimentally measurable? Because diffusion within the connected network for bound molecules is generally much slower than for unbound molecules, the essential requirement for this pathway to dominate is that the mesh size of the percolated network be comparable or larger than the size of the molecule of interest, ensuring a sufficiently high concentration of high-mobility species. It has been reported that the mesh size (or correlation length) for *in vitro* reconstituted condensates of purified LAF-1 protein is about 5 nm [65], while for reconstituted

coacervates composed of two oppositely charged intrinsically disordered proteins, histone H1 and prothymosin- α , it is about 3 nm [66]. More generally, we established a quantitative relationship between mesh size and concentration in a recent work, which suggests that condensates at physiologically relevant concentrations of 100 – 400 mg/ml exhibit mesh sizes ranging from 8 to 3 nm [67]. Since protein sizes span the reported mesh size range, we expect the new pathway to be relevant to the exchange dynamics of many condensate systems, especially for condensates of low scaffold molecule concentrations and for clients of small sizes.

Fascinating soft matter systems in their own right, biomolecular condensates are also increasingly implicated in cellular physiology and disease [68, 69]. We hope that our work will motivate further theoretical and experimental investigations into the complex dynamics in multi-component, multi-state condensates, shedding light on their functional roles and paving the way for applications in condensate bioengineering.

ACKNOWLEDGEMENTS

R.K. and Y.Z. were supported by a startup fund at Johns Hopkins University. E.K. acknowledges support from Sloan Foundation grant 138412 to R.S. and NIH grant T32GM080189. R.S. acknowledges support from Sloan Foundation grant 138412, DOE BES award DESC0010426 and NSF FET-2107246, ONR N00014-23-1-2868, and Kent Gordon Croft Investment Management Faculty Scholar fund.

* Contact authors: rkliegm1@jhu.edu (R.K.); yaojunz@jhu.edu (Y.Z.)

- [1] S. F. Banani, H. O. Lee, A. A. Hyman, and M. K. Rosen, Biomolecular condensates: organizers of cellular biochemistry, *Nat. Rev. Mol. Cell Biol.* **18**, 285 (2017).
- [2] Y. Shin and C. P. Brangwynne, Liquid phase condensation in cell physiology and disease, *Science* **357**, eaaf4382 (2017).
- [3] I. I. Cisse, I. Izeddin, S. Z. Causse, L. Boudarene, A. Senecal, L. Muresan, C. Dugast-Darzacq, B. Hajj, M. Dahan, and X. Darzacq, Real-time dynamics of RNA polymerase II clustering in live human cells, *Science* **341**, 664 (2013).
- [4] B. R. Sabari, A. Dall'Agnese, A. Boija, I. A. Klein, E. L. Coffey, K. Shrinivas, B. J. Abraham, N. M. Hannett, A. V. Zamudio, J. C. Manteiga, C. H. Li, Y. E. Guo, D. S. Day, J. Schuijers, E. Vasile, S. Malik, D. Hnisz, T. I. Lee, I. I. Cisse, R. G. Roeder, P. A. Sharp, A. K. Chakraborty, and R. A. Young, Coactivator condensation at super-enhancers links phase separation and gene control, *Science* **361**, eaar3958 (2018).
- [5] T. Hirose, K. Ninomiya, S. Nakagawa, and T. Yamazaki, A guide to membraneless organelles and their various

- roles in gene regulation, *Nat. Rev. Mol. Cell Biol.* **24**, 288 (2023).
- [6] P. Li, S. Banjade, H.-C. Cheng, S. Kim, B. Chen, L. Guo, M. Llaguno, J. V. Hollingsworth, D. S. King, S. F. Banani, *et al.*, Phase transitions in the assembly of multivalent signalling proteins, *Nature* **483**, 336 (2012).
- [7] H. Wu, Higher-order assemblies in a new paradigm of signal transduction, *Cell* **153**, 287 (2013).
- [8] X. Su, J. A. Ditlev, E. Hui, W. Xing, S. Banjade, J. Okrut, D. S. King, J. Taunton, M. K. Rosen, and R. D. Vale, Phase separation of signaling molecules promotes T cell receptor signal transduction, *Science* **352**, 595 (2016).
- [9] A. Molliex, J. Temirov, J. Lee, M. Coughlin, A. P. Kanagaraj, H. J. Kim, T. Mittag, and J. P. Taylor, Phase separation by low complexity domains promotes stress granule assembly and drives pathological fibrillization, *Cell* **163**, 123 (2015).
- [10] A. Patel, H. O. Lee, L. Jawerth, S. Maharana, M. Jahnke, M. Y. Hein, S. Stoykov, J. Mahamid, S. Saha, T. M. Franzmann, A. Pozniakovski, I. Poser, N. Maghelli, L. A. Royer, M. Weigert, E. W. Myers, S. Grill, D. Drechsel, A. A. Hyman, and S. Alberti, A liquid-to-solid phase transition of the ALS protein FUS accelerated by disease mutation, *Cell* **162**, 1066 (2015).
- [11] G. Gaglia, R. Rashid, C. Yapp, G. N. Joshi, C. G. Li, S. L. Lindquist, K. A. Sarosiek, L. Whitesell, P. K. Sorger, and S. Santagata, HSF1 phase transition mediates stress adaptation and cell fate decisions, *Nat. Cell Biol.* **22**, 151 (2020).
- [12] S. Wegmann, B. Eftekharzadeh, K. Tepper, K. M. Zoltowska, R. E. Bennett, S. Dujardin, P. R. Laskowski, D. MacKenzie, T. Kamath, C. Commins, C. Vanderburg, A. D. Roe, Z. Fan, A. M. Molliex, A. Hernandez-Vega, D. Muller, A. A. Hyman, E. Mandelkow, J. P. Taylor, and B. T. Hyman, Tau protein liquid-liquid phase separation can initiate tau aggregation, *EMBO J.* **37**, e98049 (2018).
- [13] S. Alberti and A. A. Hyman, Biomolecular condensates at the nexus of cellular stress, protein aggregation disease and ageing, *Nat. Rev. Mol. Cell Biol.* **22**, 196 (2021).
- [14] J. Nam and Y. Gwon, Neuronal biomolecular condensates and their implications in neurodegenerative diseases, *Front. Aging Neurosci.* **15**, 1145420 (2023).
- [15] S. Spann, M. Tereshchenko, G. J. Mastromarco, S. J. Ihn, and H. O. Lee, Biomolecular condensates in neurodegeneration and cancer, *Traffic* **20**, 890 (2019).
- [16] A. Boija, I. A. Klein, and R. A. Young, Biomolecular condensates and cancer, *Cancer Cell* **39**, 174 (2021).
- [17] K. Taniue and N. Akimitsu, Aberrant phase separation and cancer, *FEBS J.* **289**, 17 (2022).
- [18] X. Tong, R. Tang, J. Xu, W. Wang, Y. Zhao, X. Yu, and S. Shi, Liquid-liquid phase separation in tumor biology, *Signal Transduct. Target. Ther.* **7**, 221 (2022).
- [19] C. P. Brangwynne, C. R. Eckmann, D. S. Courson, A. Rybarska, C. Hoege, J. Gharakhani, F. Jülicher, and A. A. Hyman, Germline P granules are liquid droplets that localize by controlled dissolution/condensation, *Science* **324**, 1729 (2009).
- [20] S. An, R. Kumar, E. D. Sheets, and S. J. Benkovic, Reversible compartmentalization of de novo purine biosynthetic complexes in living cells, *Science* **320**, 103 (2008).
- [21] A. M. Pedley, J. P. Boylan, C. Y. Chan, E. L. Kennedy, M. Kyoung, and S. J. Benkovic, Purine biosynthetic enzymes assemble into liquid-like condensates dependent on the activity of chaperone protein HSP90, *J. Biol. Chem.* **298**, 101845 (2022).
- [22] M. Prouteau and R. Loewith, Regulation of cellular metabolism through phase separation of enzymes, *Biomolecules* **8**, 160 (2018).
- [23] H. Wang, F. M. Kelley, D. Milovanovic, B. S. Schuster, and Z. Shi, Surface tension and viscosity of protein condensates quantified by micropipette aspiration, *Biophys. Rep.* **1**, 100011 (2021).
- [24] I. Lifshitz and V. Slyozov, The kinetics of precipitation from supersaturated solid solutions, *J. Phys. Chem. Solid* **19**, 35 (1961).
- [25] C. Wagner, Theorie der alterung von niederschlägen durch umlösen (ostwald-reifung), *Zeitschrift Für Elektrochemie Berichte Der Bunsengesellschaft Für Phys. Chemie* **65**, 581 (1961).
- [26] M.-M. Poo and R. A. Cone, Lateral diffusion of rhodopsin in necturus rods, *Exp. Eye Res.* **17**, 503 (1973).
- [27] P. Liebman and G. Entine, Lateral diffusion of visual pigment in photoreceptor disk membranes, *Science* **185**, 457 (1974).
- [28] J. Lippincott-Schwartz, E. Snapp, and A. Kenworthy, Studying protein dynamics in living cells, *Nat. Rev. Mol. Cell Biol.* **2**, 444 (2001).
- [29] F. Pincet, V. Adrien, R. Yang, J. Delacotte, J. E. Rothman, W. Urbach, and D. Tareste, FRAP to characterize molecular diffusion and interaction in various membrane environments, *PLOS ONE* **11**, 1 (2016).
- [30] K. A. Burke, A. M. Janke, C. L. Rhine, and N. L. Fawzi, Residue-by-residue view of *in vitro* FUS granules that bind the C-terminal domain of RNA polymerase II, *Mol. Cell* **60**, 231 (2015).
- [31] S. F. Banani, A. M. Rice, W. B. Peeples, Y. Lin, S. Jain, R. Parker, and M. K. Rosen, Compositional control of phase-separated cellular bodies, *Cell* **166**, 651 (2016).
- [32] S. Jain, J. R. Wheeler, R. W. Walters, A. Agrawal, A. Barsic, and R. Parker, ATPase-modulated stress granules contain a diverse proteome and substructure, *Cell* **164**, 487 (2016).
- [33] W. M. J. Aumiller, F. Pir Cakmak, B. W. Davis, and C. D. Keating, RNA-based coacervates as a model for membraneless organelles: Formation, properties, and interfacial liposome assembly, *Langmuir* **32**, 10042 (2016).
- [34] N. O. Taylor, M.-T. Wei, H. A. Stone, and C. P. Brangwynne, Quantifying dynamics in phase-separated condensates using fluorescence recovery after photobleaching, *Biophys. J.* **117**, 1285 (2019).
- [35] L. Hubatsch, L. M. Jawerth, C. Love, J. Bauermann, T. D. Tang, S. Bo, A. A. Hyman, and C. A. Weber, Quantitative theory for the diffusive dynamics of liquid condensates, *eLife* **10**, e68620 (2021).
- [36] S. Bo, L. Hubatsch, J. Bauermann, C. A. Weber, and F. Jülicher, Stochastic dynamics of single molecules across phase boundaries, *Phys. Rev. Res.* **3**, 043150 (2021).
- [37] F. Muzzopappa, J. Hummert, M. Anfossi, S. A. Tashev, D.-P. Herten, and F. Erdel, Detecting and quantifying liquid-liquid phase separation in living cells by model-free calibrated half-bleaching, *Nat. Commun.* **13**, 7787 (2022).
- [38] A. W. Folkmann, A. Putnam, C. F. Lee, and G. Seydoux, Regulation of biomolecular condensates by interfacial protein clusters, *Science* **373**, 1218 (2021).

- 619 [39] C. F. Lee, Scaling law and universal drop size distribution
620 of coarsening in conversion-limited phase separation,
621 Phys. Rev. Res. **3**, 043081 (2021).
- 622 [40] H. T. Nguyen, N. Hori, and D. Thirumalai, Condensates
623 in RNA repeat sequences are heterogeneously organized
624 and exhibit reptation dynamics, Nat. Chem. **14**,
625 775 (2022).
- 626 [41] Y. Zhang, A. G. Pyo, R. Kliegman, Y. Jiang, C. P.
627 Brangwynne, H. A. Stone, and N. S. Wingreen, The exchange
628 dynamics of biomolecular condensates, eLife **12**,
629 RP91680 (2024).
- 630 [42] L. Hubatsch, S. Bo, T. S. Harmon, A. A. Hyman,
631 C. A. Weber, and F. Jülicher, Transport kinetics across
632 interfaces between coexisting liquid phases, bioRxiv
633 10.1101/2024.12.20.629798 (2025).
- 634 [43] J. Wang, J.-M. Choi, A. S. Holehouse, H. O. Lee,
635 X. Zhang, M. Jahnel, S. Maharana, R. Lemaitre, A. Pozniakovsky,
636 D. Drechsel, I. Poser, R. V. Pappu, S. Alberti, and A. A. Hyman,
637 A molecular grammar governing the driving forces for phase
638 separation of prion-like RNA binding proteins, Cell **174**,
639 688 (2018).
- 640 [44] G. M. Ginell and A. S. Holehouse, An introduction to the
641 stickers-and-spacers framework as applied to biomolecular
642 condensates, in *Phase-Separated Biomolecular Condensates: Methods and Protocols*,
643 edited by H.-X. Zhou, J.-H. Spille, and P. R. Banerjee (Springer US,
644 New York, NY, 2023) pp. 95–116.
- 645 [45] J.-M. Choi, A. S. Holehouse, and R. V. Pappu, Physical
646 principles underlying the complex biology of intracellular
647 phase transitions, Annu. Rev. Biophys. **49**, 107 (2020).
- 648 [46] T. Mittag and R. V. Pappu, A conceptual framework
649 for understanding phase separation and addressing open
650 questions and challenges, Mol. Cell **82**, 2201 (2022).
- 651 [47] Z. Shen, B. Jia, Y. Xu, J. Wessén, T. Pal, H. S. Chan,
652 S. Du, and M. Zhang, Biological condensates form percolated
653 networks with molecular motion properties distinctly different
654 from dilute solutions, eLife **12**, e81907 (2023).
- 655 [48] T. Wu, M. R. King, Y. Qiu, M. Farag, R. V. Pappu, and
656 M. D. Lew, Single-fluorogen imaging reveals distinct environmental
657 and structural features of biomolecular condensates, Nat. Phys. ,
658 1 (2025).
- 659 [49] See Supplemental Material at [URL-will-be-inserted-by-publisher]
660 for details.
- 661 [50] J. W. Cahn and J. E. Hilliard, Free energy of a nonuniform
662 system. I. interfacial free energy, J. Chem. Phys. **28**,
663 258 (1958).
- 664 [51] R. Skeel and M. Berzins, A method for the spatial discretization
665 of parabolic equations in one space variable, Siam J. Sci. Stat. Comput. **11**
666 (1990).
- 667 [52] P. M. McCall, K. Kim, M. Ruer-Gruß, J. Peychl, J. Guck,
668 A. A. Hyman, and J. Brugués, Label-free composition determination
669 for biomolecular condensates with an arbitrarily large number
670 of components, bioRxiv 10.1101/2020.10.25.352823 (2023).
- 671 [53] L. Jawerth, E. Fischer-Friedrich, S. Saha, J. Wang, T. Franzmann,
672 X. Zhang, J. Sachweh, M. Ruer, M. Ijavi, S. Saha, J. Mahamid,
673 A. A. Hyman, and F. Jülicher, Protein condensates as aging
674 maxwell fluids, Science **370**, 1317 (2020).
- 675 [54] S. Biffi, R. Cerbino, F. Bomboi, E. M. Paraboschi, R. Asselta,
676 F. Sciortino, and T. Bellini, Phase behavior and critical
677 activated dynamics of limited-valence DNA nanostars, Proc. Natl. Acad. Sci. **110**,
678 15633 (2013).
- 679 [55] Y. Sato, T. Sakamoto, and M. Takinoue, Sequence-based
680 engineering of dynamic functions of micrometer-sized DNA
681 droplets, Sci. Adv. **6**, eaba3471 (2020).
- 682 [56] B.-j. Jeon, D. T. Nguyen, G. R. Abraham, N. Conrad, D. K. Fygenson,
683 and O. A. Saleh, Salt-dependent properties of a coacervate-like,
684 self-assembled DNA liquid, Soft Matter **14**, 7009 (2018).
- 685 [57] S. Agarwal, D. Osmanovic, M. Dizani, M. A. Klocke, and E. Franco,
686 Dynamic control of DNA condensation, Nat. Commun. **15**,
687 1915 (2024).
- 688 [58] E. Kengmana, E. Ornelas-Gatdula, K.-L. Chen, and R. Schulman,
689 Spatial control over reactions via localized transcription within
690 membraneless DNA nanostar droplets, J. Am. Chem. Soc. **146**,
691 32942 (2024).
- 692 [59] K. Skipper and S. Wickham, Core-shell coacervates formed from
693 DNA nanostars, ChemRxiv 10.26434/chemrxiv-2024-07pvd (2024).
- 694 [60] D. T. Nguyen, B.-j. Jeon, G. R. Abraham, and O. A. Saleh,
695 Length-dependence and spatial structure of DNA partitioning
696 into a DNA liquid, Langmuir **35**, 14849 (2019).
- 697 [61] D. Y. Zhang and E. Winfree, Control of DNA strand displacement
698 kinetics using toehold exchange, J. Am. Chem. Soc. **131**,
699 17303 (2009).
- 700 [62] S. Do, C. Lee, T. Lee, D.-N. Kim, and Y. Shin, Engineering
701 DNA-based synthetic condensates with programmable material
702 properties, compositions, and functionalities, Sci. Adv. **8**,
703 eabj1771 (2022).
- 704 [63] S. Kent, K. Brown, C.-h. Yang, N. Alsaihati, C. Tian, H. Wang,
705 and X. Ren, Phase-separated transcriptional condensates
706 accelerate target-search process revealed by live-cell single-molecule
707 imaging, Cell Rep. **33**, 108248 (2020).
- 708 [64] S. Hao, Y. J. Lee, N. B. Goldfajn, E. Flores, J. Liang, H. Fuehrer,
709 J. Demmerle, J. Lippincott-Schwartz, Z. Liu, S. Sukenik, *et al.*,
710 YAP condensates are highly organized hubs, iScience **27**,
711 109927 (2024).
- 712 [65] M.-T. Wei, S. Elbaum-Garfinkle, A. S. Holehouse, C. C.-H. Chen,
713 M. Feric, C. B. Arnold, R. D. Priestley, R. V. Pappu, and C. P.
714 Brangwynne, Phase behaviour of disordered proteins underlying
715 low density and high permeability of liquid organelles, Nat. Chem. **9**,
716 1118 (2017).
- 717 [66] N. Galvanetto, M. T. Ivanović, A. Chowdhury, A. Sottini,
718 M. F. Nüesch, D. Nettek, R. B. Best, and B. Schuler, Extreme
719 dynamics in a biomolecular condensate, Nature **619**, 876
720 (2023).
- 721 [67] V. Grigorev, N. S. Wingreen, and Y. Zhang, Conformational
722 entropy of intrinsically disordered proteins bars intruders
723 from biomolecular condensates, PRX Life **3**, 013011 (2025).
- 724 [68] B. Wang, L. Zhang, T. Dai, Z. Qin, H. Lu, L. Zhang, and F. Zhou,
725 Liquid-liquid phase separation in human health and diseases,
726 Signal Transduct. Target. Ther. **6**, 290 (2021).
- 727 [69] D. M. Mitrea, M. Mittasch, B. F. Gomes, I. A. Klein, and M. A. Murcko,
728 Modulating biomolecular condensates: a novel approach to drug
729 discovery, Nat. Rev. Drug Discov. **21**, 841 (2022).